Journal of Hazardous Materials 169 (2009) 435–442

Contents lists available at ScienceDirect

Journal of Hazardous Materials

journal homepage: www.elsevier.com/locate/jhazmat

Using Large Eddy Simulation for understanding vented gas explosions in the presence of obstacles

Valeria Di Sarli[a], Almerinda Di Benedetto[a,*], Gennaro Russo[b]

[a] Istituto di Ricerche sulla Combustione, Consiglio Nazionale delle Ricerche (CNR), Via Diocleziano 328, 80124, Naples, Italy
[b] Dipartimento di Ingegneria Chimica, Università degli Studi di Napoli Federico II, Piazzale Tecchio 80, 80125, Naples, Italy

ARTICLE INFO

Article history:
Received 12 January 2009
Received in revised form 23 March 2009
Accepted 24 March 2009
Available online 31 March 2009

Keywords:
Large Eddy Simulation
Vented gas explosions
Obstacles

ABSTRACT

In this work, a validated Large Eddy Simulation model of unsteady premixed flame propagation is used to study the phenomenology underlying vented gas explosions in the presence of obstacles.

Computations are run of deflagrating flames in a small-scale combustion chamber closed at the bottom end and open at the opposite face. A single obstacle is centred inside the chamber. Methane–air mixtures of various compositions (ranging from lean to stoichiometric and rich), and obstacles with different area blockage ratios (30, 50 and 70%) and shapes (circular, rectangular and square cross-section in the flow direction) are investigated. All cases are initialized from stagnation.

The competition between combustion rate and venting rate allows explaining both number and intensity of the overpressure peaks observed.

1. Introduction

In gas explosions, the unsteady interaction of flame propagation, geometry and turbulent flow field drives the mechanisms and phenomena determining the explosion severity at different initial/operating conditions and geometrical parameters. The comprehension of the phenomenology underlying explosions is essential for an effective and safe engineering practice, i.e., for selecting the key conditions and parameters in the design and operation of refinery and chemical plants. To reach this goal, the use of mathematical models may be profitable. Among all models, Computational Fluid Dynamics (CFD) is a promising tool owing to its ability to simulate *more physics* in explosions than simple empirical or lumped-parameter models [1].

In our previous works, it has been demonstrated how CFD models based on the Unsteady Reynolds-Averaged Navier-Stokes (URANS) equations may help in understanding gas explosions [2,3]. Two configurations have been analyzed which are those of the *ducted venting* [2] and *pressure piling* [3] phenomena. In both cases, *ad hoc* simulations have allowed to identify the most relevant mechanisms influencing the pressure build-up during the flame propagation. For the *pressure piling* phenomenon, dimensionless numbers have also been derived to quantify the role and weight of each mechanism identified [4].

In practical applications, when explosions occur, flames propagating away from an ignition source may encounter obstacles along their path in the form of vessels, pipes, tanks, flow cross-section variations, etc. These objects disturb the flat propagation of the flame, increasing its rate of progression through the reactants and the pressure rise.

As reviewed in Ref. [1], over the years a great number of studies, both numerical and experimental, have been performed dealing with the unsteady premixed flame propagation through obstacles.

On the numerical side, a great effort has been focused on the development and validation of CFD codes. Most of the models are based on the URANS approach [5–12]. The Large Eddy Simulation (LES) technique has also been adopted, showing its ability to give more reliable predictions than URANS [13–16]. Recently, we have developed an LES model to simulate the unsteady flame propagation around three repeated obstacles in a laboratory-scale combustion chamber closed at one end [16]. The model has been thoroughly validated against detailed experimental data, resulting in a close agreement in terms of shape of the propagating flame, flame arrival times, flame speed, pressure time history and velocity vector fields ahead of the flame front.

Experiments have been conducted in a wide variety of conditions and geometrical configurations, and several phenomena have been identified: jet-like flame [11,14,16–22], increase of flame surface area and burning rate owing to the interaction between flame and obstacle-generated turbulent vortices [8,9,11,14,16–30], micro-explosions occurring during flame–vortex interactions [18,25], partial flame quenching [17,18,26,27], burning of pockets of fresh mixture formed behind the leading flame front

* Corresponding author. Tel.: +39 0817622673; fax: +39 0817622915.
E-mail addresses: valeria.disarli@irc.cnr.it (V. Di Sarli), almerinda.dibenedetto@irc.cnr.it (A. Di Benedetto), genrusso@unina.it (G. Russo).

0304-3894/$ – see front matter © 2009 Elsevier B.V. All rights reserved.
doi:10.1016/j.jhazmat.2009.03.115

[8,9,11,14,18–25,28–30]. Nevertheless, how these phenomena are linked to the mechanisms controlling the evolution of the flame structure, its speed and the overpressure, has yet to be clarified.

The aim of the present paper is to gain insight into the nature of the different mechanisms and phenomena coming into play during obstacle-induced explosions, identifying those controlling the development of the overpressure time history. To this end, Large Eddy Simulations are run of unsteady premixed flame propagation around an obstacle in a vented chamber. Methane–air mixtures of various compositions, and obstacles with different area blockage ratios and shapes are investigated, thus quantifying the role of the mechanisms and phenomena identified.

2. The Large Eddy Simulation (LES) model

The Large Eddy Simulation (LES) model used here has been described and validated previously [16].

Briefly, the model equations are obtained by applying a Favre-filter (i.e., a mass-weighted filter) to the Navier-Stokes equations for conservation of mass, momentum, energy and species, coupled to the constitutive and state equations.

The species transport equation is recast in the form of a transport equation for the reaction progress variable, c, which is zero within fresh reactants and unity within burned products [31]:

$$c = 1 - \frac{Y_f}{Y_f^o} \tag{1}$$

In Eq. (1), Y_f is the local fuel mass fraction and Y_f^o is the fuel mass fraction in the unburned mixture. The conservation equation for c reads as follows:

$$\frac{\partial \rho c}{\partial t} + \nabla \cdot (\rho u c) = \nabla \cdot (\rho D \nabla c) + \dot{\omega}_c \tag{2}$$

In Eq. (2), the two left hand-side terms correspond to unsteady effects and convective fluxes, while the two right hand-side terms correspond to molecular diffusion and reaction rate.

The filtering process filters out the turbulent structures whose scales are smaller than the filter width so that the resulting equations govern the dynamics of the large-scale structures. However, owing to the non-linear nature of the conservation equations, the filtering operation gives rise to unknown terms that have to be modeled at the sub-grid scale (sgs) level [32].

The unknown terms arising from the momentum equation and the energy equation are the sgs stress tensor and the sgs heat flux, respectively.

The LES Favre-filtered c-equation is written as:

$$\frac{\partial \bar{\rho}\tilde{c}}{\partial t} + \nabla \cdot (\bar{\rho}\tilde{u}\tilde{c}) + \nabla \cdot [\bar{\rho}(\widetilde{uc} - \tilde{u}\tilde{c})] = \overline{\nabla \cdot (\rho D \nabla c)} + \bar{\dot{\omega}}_c \tag{3}$$

where the overbar $(-)$ denotes a filtered quantity and the tilde $(\sim)$ a Favre-filtered quantity. In Eq. (3), there are three unknown terms: the sgs reaction progress variable flux (third term on the left hand-side), the sgs molecular diffusion (first term on the right hand-side) and the sgs reaction rate (second term on the right hand-side).

2.1. Sub-grid scale (sgs) models

The closure of the sgs stress tensor is here achieved with the dynamic Smagorinsky–Lilly eddy viscosity model [33]. After formulating a scale-similarity assumption, the model coefficients are dynamically calculated during the LES computations by using the information about the local instantaneous flow conditions provided by the smaller scales of the resolved (known) field. This allows the eddy viscosity to properly respond to the local flow structures.

The sgs fluxes of heat and reaction progress variable are modeled through the gradient hypothesis [32], along with the sgs turbulent Schmidt and Prandtl numbers assumed to be constant and equal to 0.7 [34].

To handle the flame–turbulence interaction, the flame surface density formalism based on the flamelet concept is here chosen [32]. Accordingly, the filtered molecular diffusion and reaction rate (right hand-side terms in Eq. (3)) are both included in an sgs flame front displacement term, $\overline{\rho w |\nabla c|}$, expressed as:

$$\overline{\rho w |\nabla c|} = \overline{\nabla \cdot (\rho D \nabla c)} + \bar{\dot{\omega}}_c = \left\langle \rho w \right\rangle_S \Sigma \tag{4}$$

where Σ is the sgs flame surface density (i.e., the sgs flame surface per unit volume) and $\left\langle \rho w \right\rangle_S$ is the surface-averaged mass-weighted displacement speed.

In Eq. (4), $\left\langle \rho w \right\rangle_S$ is approximated by $\rho_0 S_l$ [35], where ρ_0 is the fresh gas density and S_l is the laminar burning velocity. Σ is expressed as a function of the sgs flame wrinkling factor, Ξ_Δ (i.e., the sgs flame surface divided by the projection of the flame surface in the propagating direction):

$$\overline{\rho w |\nabla c|} = \left\langle \rho w \right\rangle_S \Sigma = \rho_0 S_l \Xi_\Delta |\nabla \tilde{c}| \tag{5}$$

In Eq. (5), Ξ_Δ is modeled according to the sgs combustion model by Charlette et al. [36] to take into account the effects of the sgs turbulence in wrinkling the flame front (in LES, the large-scale turbulence and its effects on the flame surface area are directly simulated). This sgs combustion model neglects wrinkling and corrugation produced by the interaction between the propagating flame and the acoustic waves reflected by the walls and/or objects in the combustion chamber. It has been found that this kind of interaction, which can lead to a number of instability processes, is critical in large-scale explosion tests (length of the combustion chamber of the order of meters) [37], where the acoustic time (chamber length divided by sound speed) is comparable with the combustion time (thermal diffusion divided by typical burning velocity^2). In the present work, explosions occurring in a small-scale combustion chamber are simulated.

2.2. Configuration and conditions

Fig. 1 shows a schematic representation of the combustion chamber that is a 150 mm × 150 mm × 500 mm volume, closed at the bottom end and open at the opposite face. A single obstacle is centred inside the chamber at 100 mm downstream from the bottom end.

In the base case configuration, the obstacle has a rectangular (75 mm × 12 mm) cross-section in the flow direction, and imposes an area blockage ratio equal to 50%. The chamber is filled with a stoichiometric ($\phi = 1$) mixture of methane in air.

LES computations are also run at different methane–air mixture compositions (lean, $\phi = 0.8$, and rich, $\phi = 1.2$), and obstacle blockage ratios (30 and 70%) and shapes (circular and square cross-section).

In all cases, the mixture is ignited at the centre of the bottom face (Fig. 1), starting from rest. For each run, the overpressure time history is registered in a monitor point placed at the bottom end of the chamber, close to the ignition zone (Fig. 1).

2.3. Numerical solution and problem formulation

The model equations are discretised using a finite volume formulation on a tri-dimensional non-uniform structured grid composed of around 650,000 hexahedral cells, with minimum and maximum resolutions equal to 2 mm and 3 mm, respectively. Smaller cell size is used close to the walls owing to the presence of steeper gradients of the solution field.

For the spatial discretisation of the model equations, second order bounded central schemes are chosen. The time integration

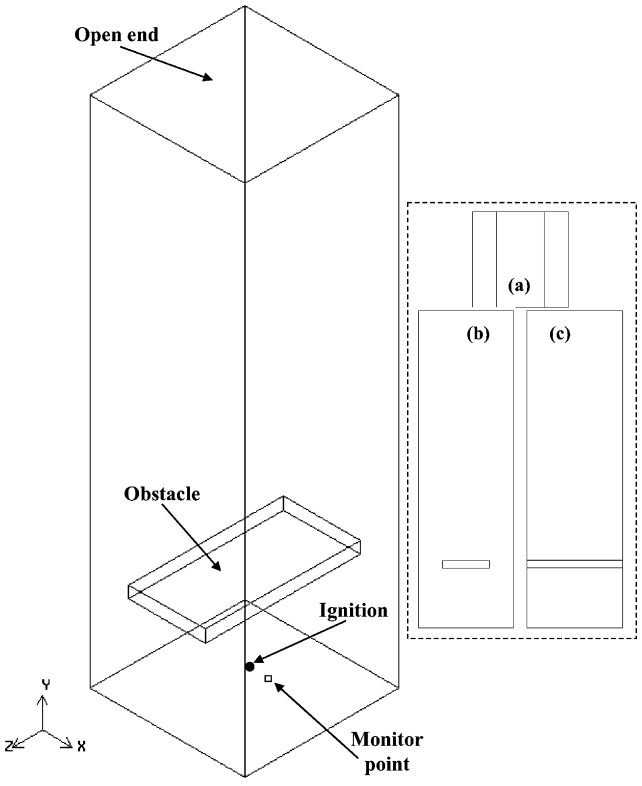

Fig. 1. Schematic diagram of the explosion chamber; in the dotted box, indications are given about the top (a), x–y (b) and y–z (c) views.

is performed by using the second order implicit Crank-Nicholson scheme.

Adiabatic and no-slip wall boundary conditions are applied at the solid interfaces (bottom and vertical faces of the chamber, faces of the obstacle). To calculate the shear stress at the wall, a blended linear/logarithmic law-of-the-wall is used [38].

Outside the combustion chamber, the computational domain is extended to simulate the presence of a dump vessel. A condition of fixed static pressure (=1.013×10^5 Pa) is specified at the boundaries of this additional domain whose distance from the exit section of the chamber (750 mm in each direction) allows minimizing the interference between the reflected pressure waves and the pressure field inside the chamber.

Initial conditions have velocity components, energy and reaction progress variable set to zero everywhere. Ignition is obtained by means of a hemispherical patch, with a radius equal to 5 mm, of hot combustion products at the centre of the bottom end.

The specific heats of the unburned and burned mixtures are approximated as piecewise fifth-power polynomial functions of temperature. The molecular viscosities are calculated according to Sutherland's law for air viscosity. The laminar burning velocity is assumed to be constant with pressure and temperature and equal to 0.28 m/s at $\phi = 0.8$, 0.41 m/s at $\phi = 1$, and 0.365 m/s at $\phi = 1.2$ [39,40].

Computations are performed by means of the segregated solver of the Fluent code (version 6.3.26) [41] adopting the SIMPLE method to treat the pressure–velocity coupling. The code is parallelized on a 64 bit computing Beowulf cluster consisting of 8 dual-CPU nodes (16 processors) each of them being an AMD Opteron 260 with 2 GB of RAM. The solution for each time step requires around 20 iterations to converge with the residual of each equation smaller than 6.0×10^{-4}. For the base case, the time needed to complete the run is about 33 h.

3. Results and discussion

In the following, the base case results are first presented. The mechanisms and phenomena leading to the overpressure peaks observed are then investigated, also by running *ad hoc* simulations. Finally, the weight and role of these mechanisms and phenomena are quantified at changing some relevant parameters.

3.1. Base case results

For the base case, Fig. 2 shows the vorticity magnitude maps as calculated on the iso-surface $c = 0.9$ (i.e., the iso-surface $Y_f = 0.1\ Y_f^o$) at different time instants after initialization. The vorticity, ξ, is a measure of the rotation of a fluid element as it moves in the flow

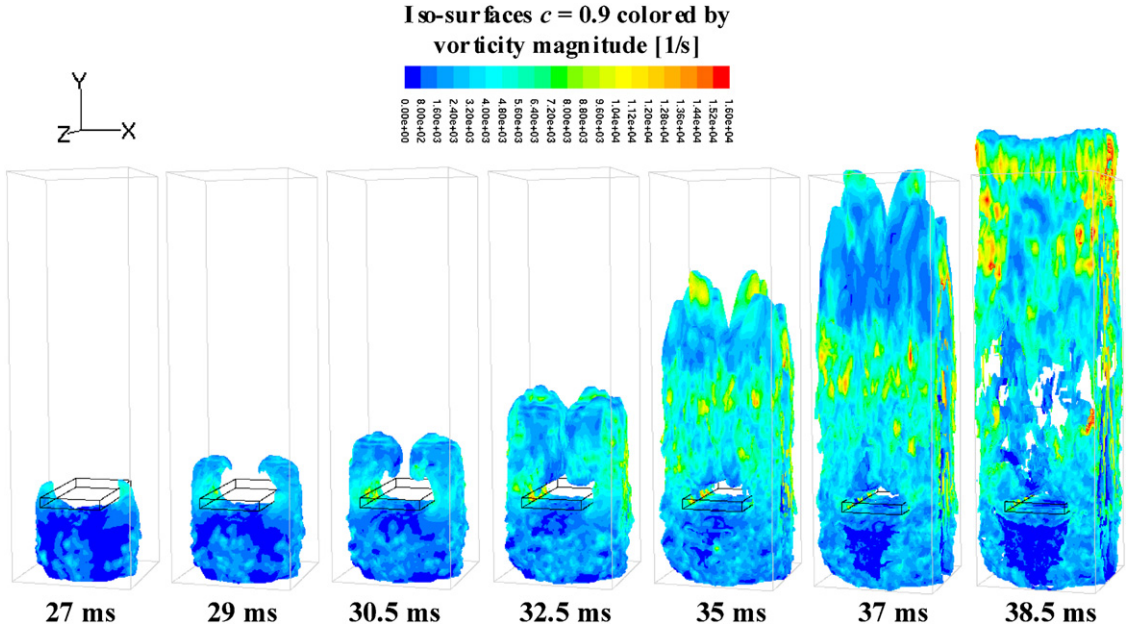

Fig. 2. Field profiles of the vorticity magnitude [1/s] on the iso-surface $c = 0.9$ at different propagation stages. Base case.

field, and is defined as the curl of the velocity vector, u:

$$\xi = \nabla \times u \tag{6}$$

Fig. 2 allows visualizing the spatio-temporal evolution of both the flame structure and the flow field encountered by the propagating flame.

When the flame reaches the obstruction, it leaves unburned mixture upstream of the obstacle and separates into two opposite flames that jet past the gaps between obstacle and chamber side walls (t = 27 ms). On exiting from the constrictions, the two flames expand and start wrapping around the vortices generated by the coupling between the unburned mixture flow, pushed ahead by the moving flame, and the obstacle itself (t = 29 ms). This flame–vortex interaction increases the degree of flame front wrinkling.

As the flames burn into the obstacle wake, they tend to reconnect with each other (29 ms $\leq t \leq$ 32.5 ms). When the reconnection is almost complete, the flame accelerates towards the vent end (t = 35 ms). At this stage, the flame exits the camber (t = 37 ms), but there are still fresh reactants in the region behind the obstacle and close to the chamber side walls. This mixture burns later on (t = 38.5 ms).

During the propagation around the obstacle, two characteristic flame speeds are observed. Along the axial direction (y), the flame propagation speed increases owing to both the cross-section decrease and the interaction with the flow field induced downstream of the obstacle. Conversely, in the x–z plane, the flame propagates much more slowly, as in a *quasi* quiescent medium. From the calculations, it results that the flame speed in the axial direction is turbulent (values up to around U_t = 20 m/s are found), while the flame speed in the planar direction is substantially laminar ($U_l \approx$ 3 m/s) owing to a much less intense turbulence, especially just behind the obstacle.

The presence of a preferential direction along the y-axis explains the reason why the flame propagates without burning the whole mixture in the chamber. Based on these results, it can be expected that the more the flame accelerates towards the chamber exit, the more the U_t/U_l ratio increases along with the amount of fresh mixture trapped inside the chamber.

Fig. 3a shows the overpressure time history as registered in correspondence to the monitor point placed at the bottom end of the chamber (Fig. 1). The overpressure trend exhibits an initial oscillating behavior with around four weak peaks ($t \leq$ 24 ms), and two later dominant peaks at about 32.5 ms and 38.5 ms.

By matching Figs. 2 and 3a, it turns out that the first main peak occurs when the two flames join with each other downstream of the obstacle. The second main peak corresponds to the combustion process of the fresh mixture remained inside the chamber when the two flames have completed their reconnection, eventually exiting the chamber.

3.1.1. Analysis of the mechanisms and phenomena

To clarify the mechanisms and phenomena that link the flame propagation to the overpressure time history, the combustion chamber is conceptually divided into two parts: the first part, which lies from the bottom face up to the obstacle, and the second part, which lies from the obstacle up to the chamber exit (Fig. 3d).

Each chamber is vented: the first chamber towards the second chamber, and this latter towards the external environment.

The overpressure peaks shown in Fig. 3a are addressed to the competition between two counteracting phenomena that occur in both chambers, combustion rate and venting rate:

$$\Delta P_{\max} = f\left(\frac{\text{Combustion rate}}{\text{Venting rate}}\right) \tag{7}$$

The combustion rate promotes the pressure increase through the production and accumulation of burned gas. Conversely, the venting rate promotes the pressure decrease by emptying the chamber.

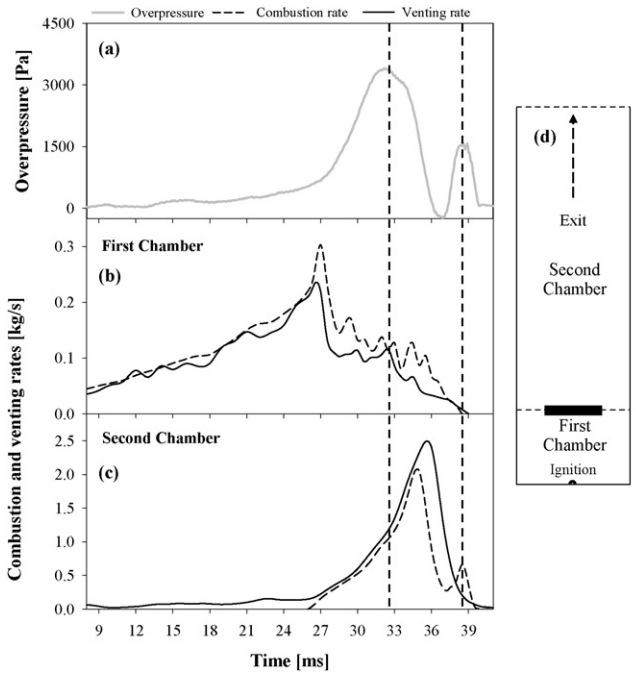

Fig. 3. Overpressure time history at the bottom end of the combustion chamber (a); time trends of the combustion and venting rates in the first (b) and second (c) chambers; conceptual division of the combustion chamber (d). Base case.

The goal here is to illustrate what mechanism drives the f function in Eq. (7), thus relating the phenomena occurring in the combustion chamber to the overpressure time trend.

Fig. 3b and c shows the time histories of the combustion rate for the first (Fig. 3b) and second (Fig. 3c) chambers. In these figures, the time trends of the venting rates are also shown. The venting rates are computed as mass flow rate of the gas exiting the obstacle mid-height section and the channel outlet section for the first chamber (Fig. 3b) and the second chamber (Fig. 3c), respectively.

When the flame is all upstream of the obstacle (i.e., in the first chamber, $t \leq$ 24 ms), the combustion chamber is efficiently vented, given that the combustion rate and the venting rates at both, the obstacle section and the chamber exit section, assume very close values. As a result, the chamber overpressure does not significantly increase. Furthermore, a weakly oscillating time behavior of the venting rate from the first chamber can be noted in Fig. 3b, which is responsible for the four weak peaks observed in the corresponding overpressure trend.

Starting from around 27 ms after initialization, the venting rate from the first chamber decreases. At this time instant, the flame reaches the obstacle and starts to flow around it, accelerating rapidly. In these conditions, the passage between obstacle and chamber walls is obstructed by the here-defined *obstacle-side combustion*, while fresh mixture has yet to be burned in the first chamber (Fig. 2). Consequently, up to around 32.5 ms, the flame propagates in the first chamber as in an almost closed vessel.

Fig. 3c also shows that, during this propagation phase, the combustion and venting rates in the second chamber follow each other: the increasing chamber pressure and hence the increasing pressure drop promote the venting rate towards the exit. Indeed, the burned gases produced by the obstacle-accelerated flame almost instantaneously flow out of the chamber.

As a result, the first main peak has to be ascribed to the *obstacle-side combustion* that acts on the flame propagation in the first chamber as an external explosion of a simply vented configuration [42].

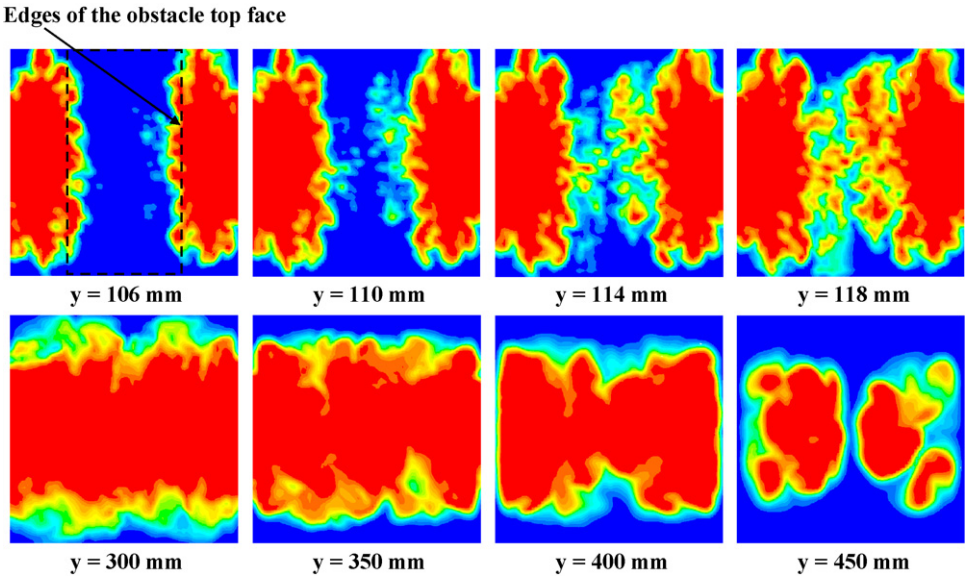

Fig. 4. Reaction progress variable maps as computed at different x–z planes when the flame exits the chamber (t = 37 ms). Base case.

After the first peak, combustion mainly proceeds in the second chamber. The second overpressure peak is again the result of the coupling between combustion rate and venting rate. Before this peak, the flame exiting the combustion chamber leaves unburned mixture accumulated inside the chamber. This gives rise to a *pseudo-confined combustion* whose occurrence is manifested by the peak in the combustion rate shown in Fig. 3c. On the other hand, the venting rate decreases, given that the flame reaches the chamber exit, producing an external explosion of the fresh gas pushed outside by the propagating front itself. The flame rapidly expands in the external environment and thus the maximum overpressure associated to this explosion is rather limited (less than 300 Pa, close to the chamber exit). The main effect of this phenomenon is to temporary block the venting rate from the second chamber. Consequently, the *pseudo-confined combustion* of the reactants trapped inside the chamber occurs with a significantly decreased venting rate, leading to the second overpressure peak.

In summary, the first main peak is caused by the *obstacle-side combustion*, while the second main peak is caused by the *pseudo-confined combustion* phenomenon.

3.1.2. Ad hoc simulations for studying the pseudo-confined combustion phenomenon

In most of the literature works dealing with the unsteady flame propagation in configurations similar to that examined here, the overpressure peaks observed are explained by violent combustion of the fresh mixture trapped behind the obstacle [10,13–15,20,21,29].

In Fig. 4, the reaction progress variable maps are shown as computed at different x–z planes along the combustion chamber when the flame exits the chamber (t = 37 ms). From this figure, it is possible to quantify the unburned mixture to burned mixture ratio over the cross-section of the camber at different axial positions.

Fig. 4 shows that a relevant amount of unburned mixture remains accumulated inside the chamber, behind the obstacle (106 mm $\leq y \leq$ 118 mm) and close to the chamber side walls. As already observed, this is a consequence of the bi-directional behavior of the flame propagation: owing to the presence of the obstacle, the flame speed in the x–z plane is much lower than the flame speed in the perpendicular (y) direction.

In order to weigh the role of the mixture trapped behind the obstacle in relation to that of the mixture accumulated close to the chamber walls, *ad hoc* simulations are run by assuming the mixture trapped behind the obstacle as burned. This is obtained through an initial (t = 0 ms) patch of burned products downstream of the obstacle.

In Fig. 5, the overpressure time trend is plotted for both the modified case (MC) and the original case (OC).

Fig. 5 shows that, in the absence of the unburned mixture behind the obstacle, the second overpressure peak occurs at the same time instant ($t \approx$ 38.5 ms) and is slightly lower than the original peak (1500 Pa *versus* 1800 Pa). This means that the second peak has to be mainly addressed to the combustion process of the fresh mixture remained close to the chamber side walls.

3.2. Effect of the parameters

In the previous sub-section, the competition between combustion rate and venting rate has been identified as the main mechanism correlating the spatio-temporal evolution of the flame structure and the overpressure time history via two phenomena, *obstacle-side combustion* and *pseudo-confined combustion*. In the present sub-section, the effects of the mechanism and phenom-

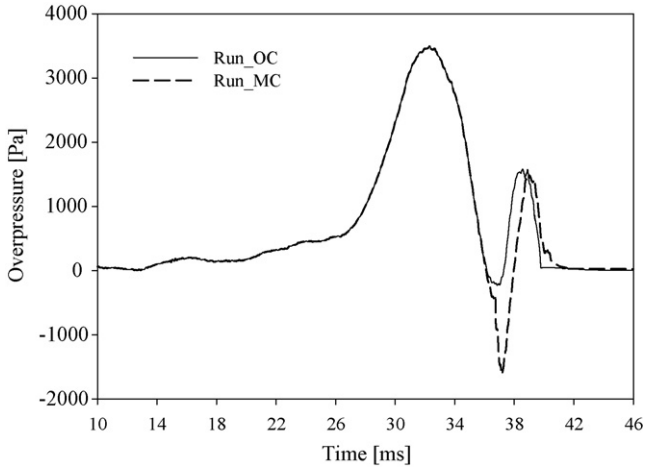

Fig. 5. Overpressure time history at the bottom end of the combustion chamber: original case (i.e., base case) (OC) and modified case (MC).

ena identified on the overpressure peaks are quantified at different fuel equivalence ratios, and obstacle blockage ratios and shapes.

3.2.1. Fuel equivalence ratio

In Fig. 6, the overpressure time histories are shown as computed at the bottom end of the chamber at different fuel equivalence ratios, $\phi = 0.8$, $\phi = 1$ (base case) and $\phi = 1.2$. The overpressure peaks become more intense and occur earlier on ranging from lean to rich and stoichiometric conditions. These trends are consistent with the literature results [12,20,21,26,27], which show that the unsteady flame propagation through obstacles is strongly dependent on the fuel equivalence ratio, and the highest flame speeds and overpressures are found at stoichiometric (or nearly stoichiometric, i.e., slightly rich) conditions.

From Fig. 6 it can be seen that, as the stoichiometric propagation case, the rich case exhibits two dominant overpressure peaks. Conversely, with the lean flame, four peaks can be observed.

At each equivalence ratio, the first peak corresponds to the burning phase of the reactants remained upstream of the obstacle when the *obstacle-side combustion* occurs, thus blocking the venting rate from this chamber zone.

At rich and stoichiometric conditions, the first peak is more violent than in the lean case. This is due to the faster flame reactivity that implies both direct and indirect effects on the jet-flame. The direct effect is on the laminar flame speed itself. The indirect effect is on the turbulent flow field generated at the obstacle edges. These effects justify the trend of the *obstacle-side combustion* peak by varying the equivalence ratio.

It is worth noting that the *obstacle-side combustion* results in a single overpressure peak at rich and stoichiometric conditions, and in to two peaks at lean conditions. This may be attributed to the fact that, with a slower flame propagation, combustion and venting act with more comparable rates. As a result, these two counteracting phenomena balance each other and an almost oscillating behavior for the overpressure time trend is established.

Going further in the propagation downstream of the obstacle, again a single peak is found with the stoichiometric and rich cases, and two peaks with the lean flame. At each equivalence ratio, these peaks correspond to the *pseudo-confined combustion* of the fresh mixture trapped inside the chamber when the flame vents towards the exit, thus exploding outside. The amount of accumulated reactants is nearly the same by varying the equivalence ratio. This means that the different intensity of the *pseudo-confined combustion* peaks is due to the increase of both the flame reactivity and the turbulence level induced by the propagation itself, that leads to an ever more rapid combustion of the trapped mixture on ranging from lean to rich and stoichiometric conditions.

3.2.2. Obstacle blockage ratio

Fig. 7shows the overpressure time trends as registered close to the ignition patch at different obstacle blockage ratios, 30%, 50% (base case) and 70%. Two dominant overpressure peaks are always present whose intensity increases with the blockage ratio. This trend has also been found in a great number of literature studies [8,10,14,24,27,29,30].

On increasing the blockage ratio, the flow cross-section between obstacle and chamber side walls decreases, with a consequential increase in intensity for the jet-flame. As a result, the *obstacle-side combustion* becomes more violent and the first peak increases with the blockage ratio.

Concerning the second peak, owing to the increase of the U_t/U_l ratio, the amount of fresh mixture involved in the *pseudo-confined combustion* increases with the blockage ratio. This couples with the more intense turbulence generated by the flame-obstacle interaction, thus explaining the trend of the second peak of Fig. 7.

3.2.3. Obstacle shape

In the literature, the effect of the obstacle shape on the unsteady flame propagation and associated overpressure time trend has been

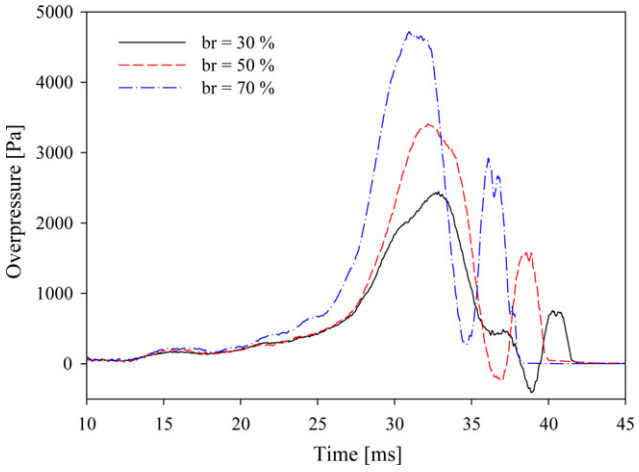

Fig. 7. Overpressure time histories taken at the bottom end of the combustion chamber at different obstacle blockage ratios.

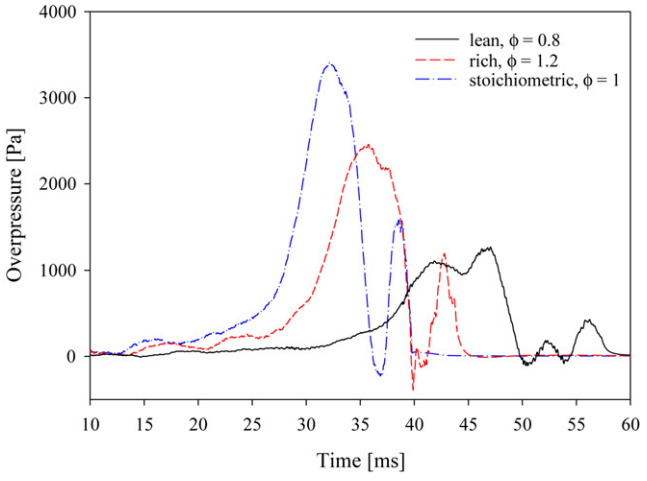

Fig. 6. Overpressure time histories taken at the bottom end of the combustion chamber at different fuel equivalence ratios.

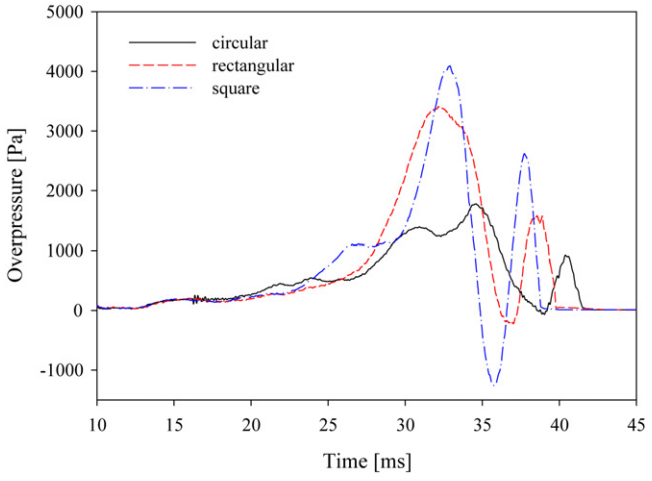

Fig. 8. Overpressure time histories taken at the bottom end of the combustion chamber at varying the shape of the obstacle cross-section in the flow direction.

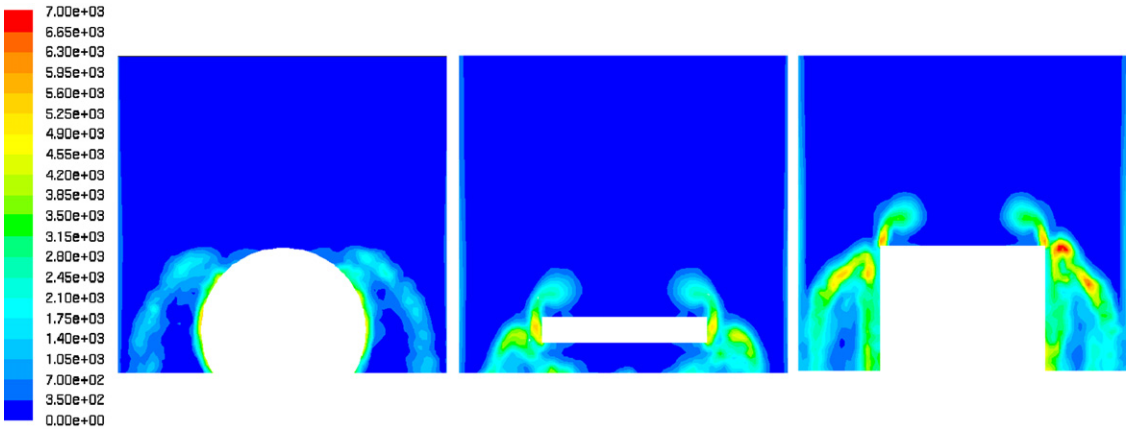

Fig. 9. Vorticity magnitude [1/s] maps as computed when the flame has covered the axial length of the obstacle at varying the shape of the obstacle cross-section in the flow direction (the maps are taken at the central *x*–*y* plane of the combustion chamber).

widely studied [10,14,19,21,29,30]. The common conclusion of these works is that obstacles with sharp-edged cross-sections in the flow direction (squares, rectangles, diamonds and triangles) give rise to a more intense flame front wrinkling, and thus higher flame accelerations, than obstacles with round-edged cross-sections (cylinders). Generally, this faster acceleration also results in higher overpressure peaks.

In Fig. 8, the overpressure time histories are shown as obtained at the bottom end of the chamber changing the shape of the obstacle cross-section, circular, rectangular (base case) and square.

With the sharp-edged obstacles (square and rectangle), the peaks are stronger than with the round-edged obstacle (cylinder). Furthermore, two peaks are found with the rectangle, and three peaks with both the square and cylinder. In these latter cases, the first peak (i.e., the *obstacle-side combustion* peak) is split into two peaks. The reason for this behavior has to be found in the fact that the axial length (i.e., the height) of the square and cylinder is greater (75 mm) than that of the rectangle (12 mm). As a result, the venting configuration established between the chamber zones upstream and downstream of the obstacle is more similar to that of a ducted venting [43] rather than to a simply vented configuration [42].

The flame reaches the square obstacle at around 23 ms after initialization. Starting from this time instant, the venting rate from the chamber zone upstream of the obstacle decreases and, hence, combustion proceeds in conditions of partially reduced venting. Correspondingly, the overpressure increases up to a first peak that occurs at around 26.5 ms.

The flame takes about 6 ms to cover the gap (i.e., the duct) between obstacle and wall. When the flame completely fills this gap, the venting rate drastically drops. Consequently, the remaining mixture, whose mass is about 50% of the initial value, burns as in an almost closed vessel. Starting from about 1100 Pa, the overpressure increases again up to the second peak found at 33 ms.

Also in the rectangle case, when the *obstacle-side combustion* occurs, the mass of fresh mixture upstream of the obstacle is around 50% of the initial value. However, the venting rate starts decreasing earlier with the square than with the rectangle. As a result, in the square case, the overpressure has the time to build-up so that the flame propagation in isolated conditions upstream of the obstacle starts from an overpressure that is higher than in the rectangle case. This pre-compression phenomenon explains the reason why the *obstacle-side combustion* leads to a higher overpressure peak with the square than with the rectangle.

As with the square, also with the cylinder the venting rate starts decreasing earlier, giving rise to a pre-compression phenomenon (first peak, $t = 31$ ms). However, differently from the square and rectangle cases, the circular shape allows the flame to wind itself round the obstacle. Consequently, the flame is not able to completely block the venting rate, thus resulting in an *obstacle-side combustion* that leads to a lower second peak ($t = 34.5$ ms) than the corresponding peaks observed with the square and rectangle.

Concerning the *pseudo-confined combustion* phenomenon, it leads to overpressure peaks of increasing intensity on ranging from the cylinder to the rectangle and square. The amount of fresh mixture involved is larger with the square. On the other hand, the turbulent flow field induced around the obstacle is strongly dependent on the obstacle shape and, in particular, on the presence of sharp or rounded edges.

For the three different shapes investigated, Fig. 9 shows the vorticity magnitude field profiles when the flame has covered the axial length of the obstacle. This figure demonstrates that a weak vortex shedding occurs with the cylinder. Moreover, the eddy generation is more intense with the square than with the rectangle.

4. Summary and conclusions

A validated Large Eddy Simulation (LES) model of unsteady premixed flame propagation has been used to study the phenomenology underlying explosions occurring in a small-scale vented chamber in the presence of a single obstacle.

The overpressure peaks observed have been attributed to the competition between combustion rate and venting rate via two main phenomena, *obstacle-side combustion* and *pseudo-confined combustion*.

The *obstacle-side combustion* occurs when the flame crosses the constrictions between obstacle and chamber side walls, accelerating rapidly and leaving unburned mixture in the chamber zone upstream of the obstruction. The *obstacle-side combustion* results in a decrease of venting rate from this portion of chamber, where combustion is thus forced to proceed as in an almost closed vessel.

The *pseudo-confined combustion* corresponds to the burning phase of the mixture that remains trapped in the chamber zone downstream of the obstacle when the flame exits the chamber. It leads to an overpressure increase by the coupling with the decrease of venting rate towards the external environment. This decrease of venting rate is due to the effect of the explosion process of the fresh mixture pushed outside and ignited by the flame jetting from the chamber.

Through *ad hoc* simulations, it has been demonstrated that the fresh mixture accumulated close to the chamber side walls has a more relevant effect on the *pseudo-confined combustion* phenomenon, and hence on the related peak, than the mixture present behind the obstacle.

The results of computations run at changing some relevant parameters have shown that the intensity of both the *obstacle-side combustion* and *pseudo-confined combustion* peaks increases on increasing the flame reactivity (i.e., on ranging from lean to rich and stoichiometric conditions) and the obstacle blockage ratio, and when using sharp-edged obstacles instead of round-edged obstacles. The number of peaks has been found to increase on decreasing the laminar burning velocity (i.e., with the lean flame) and on increasing the obstacle height (i.e., with the circular and square cross-section obstacles).

In conclusion, the LES model has demonstrated itself to be a useful tool for identifying and quantifying the mechanisms and phenomena driving the pressure build-up in a flame-flow configuration often encountered in practical gas explosions. Such identification and quantification are needed steps in the design and operation of safe industrial plants.

References

[1] V. Di Sarli, A. Di Benedetto, E. Salzano, G. Ferrara, G. Russo, Mitigation of gas explosions in industrial equipment by means of venting systems, in: P.B. Warey (Ed.), New Research on Hazardous Materials, Nova Science Publishers, New York, 2007, pp. 249–291.

[2] G. Ferrara, A. Di Benedetto, E. Salzano, G. Russo, CFD analysis of gas explosions vented through relief pipes, J. Hazard. Mater. 137 (2006) 654–665.

[3] A. Di Benedetto, E. Salzano, G. Russo, The mitigation of pressure piling by divergent connections, Process Saf. Prog. 24 (2005) 310–315.

[4] A. Di Benedetto, E. Salzano, G. Russo, Predicting pressure piling by semi-empirical correlations, Fire Saf. J. 40 (2005) 282–298.

[5] B.H. Hjertager, T. Solberg, K.O. Nymoen, Computer modelling of gas explosion propagation in offshore modules, J. Loss Prev. Process Ind. 5 (1992) 165–174.

[6] C.A. Catlin, M. Fairweather, S.S. Ibrahim, Predictions of turbulent, premixed flame propagation in explosion tubes, Combust. Flame 102 (1995) 115–128.

[7] N.R. Popat, C.A. Catlin, B.J. Arntzen, R.P. Lindstedt, B.H. Hjertager, T. Solberg, O. Saeter, A.C. Van den Berg, Investigations to improve and assess the accuracy of computational fluid dynamic based explosion models, J. Hazard. Mater. 45 (1996) 1–25.

[8] D.K. Pritchard, D.J. Freeman, P.W. Guilbert, Prediction of explosion pressures in confined spaces, J. Loss Prev. Process Ind. 9 (1996) 205–215.

[9] M. Fairweather, G.K. Hargrave, S.S. Ibrahim, D.G. Walker, Studies of premixed flame propagation in explosion tubes, Combust. Flame 116 (1999) 504–518.

[10] P. Naamansen, D. Baraldi, B.H. Hjertager, T. Solberg, S. Cant, Solution adaptive CFD simulation of premixed flame propagation over various solid obstructions, J. Loss Prev. Process Ind. 15 (2002) 189–197.

[11] S.N.D.H. Patel, S. Jarvis, S.S. Ibrahim, G.K. Hargrave, An experimental and numerical investigation of premixed flame deflagration in a semiconfined explosion chamber, Proc. Combust. Inst. 29 (2002) 1849–1854.

[12] E. Salzano, F.S. Marra, G. Russo, J.H.S. Lee, Numerical simulation of turbulent gas flames in tubes, J. Hazard. Mater. 95 (2002) 233–247.

[13] M.P. Kirkpatrick, S.W. Armfield, A.R. Masri, S.S. Ibrahim, Large eddy simulation of a propagating turbulent premixed flame, Flow Turbul. Combust. 70 (2003) 1–19.

[14] A.R. Masri, S.S. Ibrahim, B.J. Cadwallader, Measurements and large eddy simulation of propagating premixed flames, Exp. Therm. Fluid Sci. 30 (2006) 687–702.

[15] S.R. Gubba, S.S. Ibrahim, W. Malalasekera, A.R. Masri, LES modeling of premixed deflagrating flames in a small-scale vented explosion chamber with a series of solid obstructions, Combust. Sci. Technol. 180 (2008) 1936–1955.

[16] V. Di Sarli, A. Di Benedetto, G. Russo, S. Jarvis, E.J. Long, G.K. Hargrave, Large eddy simulation and PIV measurements of unsteady premixed flames accelerated by obstacles, Flow Turbul. Combust., doi:10.1007/s10494-008-9198-3, in press.

[17] R. Starke, P. Roth, An experimental investigation of flame behavior during explosions in cylindrical enclosures with obstacles, Combust. Flame 75 (1989) 111–121.

[18] N. Ardey, F. Mayinger, B. Durst, Influence of transport phenomena on the structure of lean premixed hydrogen air flames, Transac. Am. Nucl. Soc. 73 (1995).

[19] A.R. Masri, S.S. Ibrahim, N. Nehzat, A.R. Green, Experimental study of premixed flame propagation over various solid obstructions, Exp. Therm. Fluid Sci. 21 (2000) 109–116.

[20] S.S. Ibrahim, G.K. Hargrave, T.C. Williams, Experimental investigation of flame/solid interactions in turbulent premixed combustion, Exp. Therm. Fluid Sci. 24 (2001) 99–106.

[21] G.K. Hargrave, S. Jarvis, T.C. Williams, A study of transient flow turbulence generation during flame/wall interactions in explosions, Meas. Sci. Technol. 13 (2002) 1036–1042.

[22] S. Jarvis, G.K. Hargrave, A temporal PIV study of flame/obstacle generated vortex interactions within a semi-confined combustion chamber, Meas. Sci. Technol. 17 (2006) 91–100.

[23] I.O. Moen, M. Donato, R. Knystautas, J.H. Lee, Flame acceleration due to turbulence produced by obstacles, Combust. Flame 39 (1980) 21–32.

[24] I.O. Moen, J.H.S. Lee, B.H. Hjertager, K. Fuhre, R.K. Eckhoff, Pressure development due to turbulent flame propagation in large-scale methane–air explosions, Combust. Flame 47 (1982) 31–52.

[25] P. Wolański, S. Wójcicki, On the mechanism of influence of obstacles on the flame propagation, Arch. Combust. 1 (1981) 69–74.

[26] B.H. Hjertager, K. Fuhre, M. Bjørkhaug, Concentration effects on flame acceleration by obstacles in large-scale methane–air and propane-air vented explosions, Combust. Sci. Technol. 62 (1988) 239–256.

[27] H. Phylaktou, G.E. Andrews, The acceleration of flame propagation in a tube by an obstacle, Combust. Flame 85 (1991) 363–379.

[28] R.P. Lindstedt, V. Sakthitharan, Time resolved velocity and turbulence measurements in turbulent gaseous explosions, Combust. Flame 114 (1998) 469–483.

[29] S.S. Ibrahim, A.R. Masri, The effects of obstructions on overpressure resulting from premixed flame deflagration, J. Loss Prev. Process Ind. 14 (2001) 213–221.

[30] D.J. Park, A.R. Green, Y.S. Lee, Y.-C. Chen, Experimental studies on interactions between a freely propagating flame and single obstacles in a rectangular confinement, Combust. Flame 150 (2007) 27–39.

[31] P.A. Libby, F.A. Williams (Eds.), Turbulent Reacting Flows, Academic Press, New York, 1994.

[32] T. Poinsot, D. Veynante, Theoretical, Numerical Combustion, second ed., R.T. Edwards, Philadelphia, 2005.

[33] D.K. Lilly, A proposed modification of the Germano subgrid-scale closure method, Phys. Fluids A 4 (1992) 633–635.

[34] L.G. Loitsyanskiy, Mechanics of Liquids and Gases, sixth ed., Begell House, New York, 1995.

[35] A. Trouvé, T. Poinsot, The evolution equation for the flame surface density in turbulent premixed combustion, J. Fluid Mech. 278 (1994) 1–31.

[36] F. Charlette, C. Meneveau, D. Veynante, A power-law flame wrinkling model for LES of premixed turbulent combustion. Part I. Non-dynamic formulation and initial tests, Combust. Flame 131 (2002) 159–180.

[37] O.J. Teerling, A.C. McIntosh, J. Brindley, V.H.Y. Tam, Premixed flame response to oscillatory pressure waves, Proc. Combust. Inst. 30 (2005) 1733–1740.

[38] S.-E. Kim, Large eddy simulation using unstructured meshes and dynamic subgrid-scale turbulence models, AIAA Paper (2004), AIAA-2004-2548.

[39] G. Yu, C.K. Law, C.K. Wu, Laminar flame speeds of hydrocarbon + air mixtures with hydrogen addition, Combust. Flame 63 (1986) 339–347.

[40] V. Di Sarli, A. Di Benedetto, Laminar burning velocity of hydrogen–methane/air premixed flames, Int. J. Hydrogen Energy 32 (2007) 637–646.

[41] Fluent 6.3.26, Fluent Inc., Lebanon, NH (USA), website: <www.fluent.com>, 2007 (accessed 18.12.08).

[42] A.J. Harrison, J.A. Eyre, "External explosions" as a result of explosion venting, Combust. Sci. Technol. 52 (1987) 91–106.

[43] M.G. Cooper, M. Fairweather, J.P. Tite, On the mechanisms of pressure generation in vented explosions, Combust. Flame 65 (1986) 1–14.